UC Santa Cruz

UC Santa Cruz Previously Published Works

Title

Deep low-frequency tremor that correlates with passing surface waves

Permalink

https://escholarship.org/uc/item/65x691k6

Journal

Journal of Geophysical Research, 113(B01307)

Authors

Miyazawa, Masatoshi
Brodsky, Emily E.

Publication Date

2008-01-24

Peer reviewed

eScholarship.org Powered by the California Digital Library
University of California

Deep low-frequency tremor that correlates with passing surface waves

Masatoshi Miyazawa[1] and Emily E. Brodsky[2]

Received 5 December 2006; revised 23 July 2007; accepted 28 September 2007; published 24 January 2008.

[1] The large surface waves from the 2004 Sumatra-Andaman earthquake dynamically perturbed the upper mantle structure in Japan and triggered periodic deep low-frequency seismic tremor in eastern and western Shikoku, western and central Tokai, and the Kii peninsula. We use the relationship between the amplitude of the triggered tremor and the stresses of the seismic waves to investigate the mechanism of deep low-frequency seismic tremor. Volumetric strain changes from the 15–30 s Rayleigh waves play an important role in the strong triggering, likely via Coulomb failure stress changes. Building on previous results that the tremor signals become increasingly strong with increasing dilatation, we observe a clear increase in the triggered tremor with an increase in the dilatation due to the Rayleigh waves at the 30 km depth source regions. We also observe a correlation with the Coulomb failure stress change resolved on an appropriate plane. There is an exponential relationship between the signal amplitude from triggered tremor and both the dilatation and the Coulomb shear stress at the source region. This combined with the shape of the tremor packets implies that the tremor amplitude is predictable based on the amplitude of the incoming waves. The amplitude variations can be explained by a distribution of sources in the tremor source region.

Citation: Miyazawa, M., and E. E. Brodsky (2008), Deep low-frequency tremor that correlates with passing surface waves, *J. Geophys. Res.*, *113*, B01307, doi:10.1029/2006JB004890.

1. Introduction

[2] Deep low-frequency tremor on subducting slabs is a recently discovered and novel seismic signal [*Obara*, 2002]. The waves are unusually long-period for their amplitude and the signal is often continuous with little punctuation over times ranging from tens of minutes to a few days. These seismic features are often seen in volcanic regions and usually interpreted as signs of fluid-filled resonant conduits in that setting. Therefore early work on deep, slab tremor suggested a fluid source by analogy. Geochemical and petrological constraints supported the inference by suggesting that fluids are released from the subducting slab in a series of dehydration reactions at the depth of the tremor [e.g., *Toriumi and Inui*, 2001; *Omori et al.*, 2004]. The coincidence of the tremor with slow slip also suggests that there is some physical connection with the large-scale slab processes at the depth of 30–40 km.

[3] More recent work has suggested that low-frequency earthquakes and tremor can be generated by simple shear failure in both the subduction and the volcanic settings. A low rupture velocity or low-stress drop can result in the low-frequency waves and overlapping earthquakes can generate the apparently continuous signal [*Harrington and Brodsky*, 2007; *Shelly et al.*, 2006]. Still, the occurrence of the tremor and slow slip at the depth of dehydration suggests that fluids may be an important component.

[4] Here we study the origin of slab tremor by using a constraint posed by special cases of slab tremor that are triggered by the seismic waves from distant earthquakes. The 2004 Sumatra-Andaman earthquake (M_w9.2) was enormous and the surface wave amplitudes measured in Japan were comparable to or a few times as large as those from the Denali earthquake (M_w7.9) in 2002 that contributed to the well-studied earthquake triggering around North America [e.g., *Prejean et al.*, 2004]. *Miyazawa and Mori* [2006] showed that periodic triggering of deep low-frequency events in western Japan was due to the Rayleigh waves from the Sumatra earthquake, and suggested that the triggering is well correlated with the large tensile dilatation at the source regions (Figures 1 and 2). Similar triggered tremor occurred after small local earthquakes and large teleseisms [*Obara*, 2003], and during the surface waves of the 2003 Tokachi-oki earthquake (M_w8.1) [*Miyazawa and Mori*, 2005]. These initial observations were thought to distinguish the tremor from the ordinary earthquakes triggered in Alaska that were promoted by shear failure [*West et al.*, 2005]. Recently, *Rubinstein et al.* [2007] found that the bursts of similar nonvolcanic tremor in Cascadia subduction zone were triggered by Love waves from the 2002 Denali earthquake.

[5] More careful analysis of the relationship between the input strains of the seismic waves and the resultant tremor may help us untangle the mechanisms of deep-slab tremor in western Japan.

[1]Disaster Prevention Research Institute, Kyoto University, Kyoto, Japan.
[2]Department of Earth Sciences, University of California, Santa Cruz, California, USA.

Copyright 2008 by the American Geophysical Union.
0148-0227/08/2006JB004890$09.00

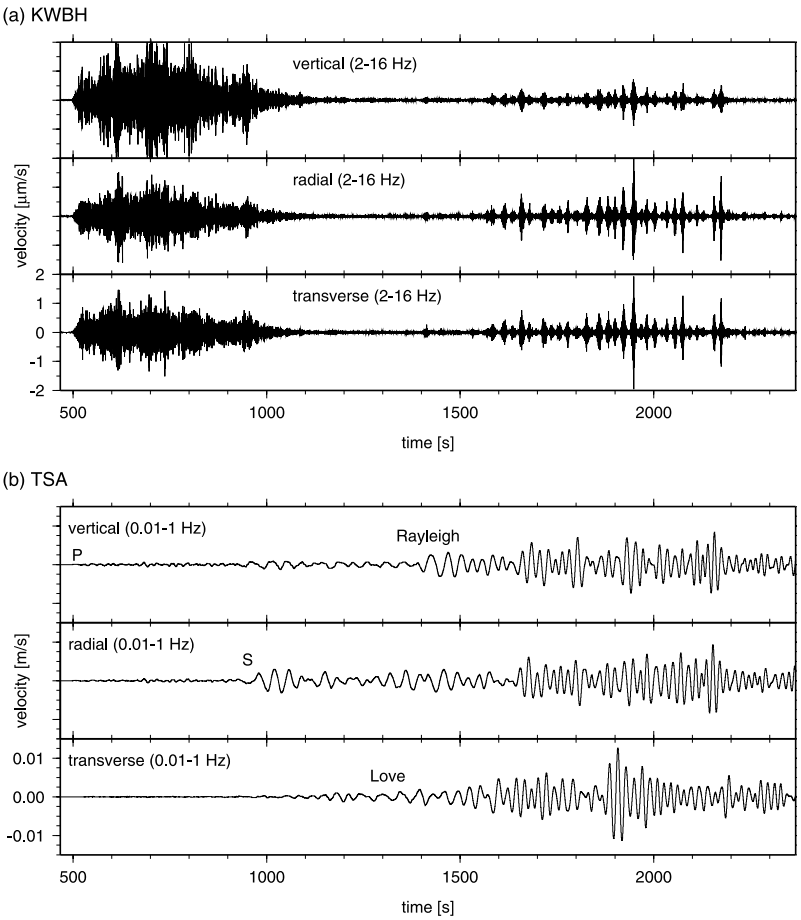

Figure 1. Observed velocity waveforms from the 2004 Sumatra-Andaman earthquake (a) filtered with a passband from 2 to 16 Hz at a borehole high sensitive station KWBH and (b) filtered with a passband from 0.01 to 1 Hz at a broadband station TSA. Zero is the origin time of the Sumatra earthquake (26 December 2004, 0058:53 UT). Three traces indicate the vertical, radial, and transverse components from the top to the bottom. The two station locations are shown in Figure 3. The epicentral distance is about 5000 km.

[6] This paper begins with a review of prior observations of triggered tremor combined with a discussion of the most salient first-order features found here. We then derive the strain changes in the tremor source regions due to the Sumatra seismic waves. By comparing the spectra of the triggered and input signals, we determine which frequencies of the surface waves are capable of significantly triggering the tremor. We proceed to more carefully investigate the functional dependence of the amplitude of the tremor given various assumptions about the spatial distribution of sources. We also examine the data's ability to resolve the orientation of the input stresses. Finally, we discuss the physical implications of our results for both an individual failure event and a distribution of sources.

2. Observations

2.1. Overview of Triggered Tremor

[7] *Miyazawa and Mori* [2006] used the High Sensitivity Seismograph Network (Hi-net) to uncover nonvolcanic deep low-frequency tremor triggered by the Sumatra earthquake. By filtering the continuous waveforms, they found discrete episodes of low-frequency tremor that correlated well with the packets of the Rayleigh waves (Figure 1). They established that volumetric expansion in the source region correlated well with the triggering (Figure 2). When the dilatation had peak values of about 10^{-7}, strong triggering was observed. (Throughout this paper, we use the convention of extension and expansion as positive strain and the term "dilatation" strictly for volumetric strain.)

[8] *Miyazawa and Mori* [2006] located the tremor using a modified envelope correlation method [*Obara*, 2002; *Miyazawa and Mori*, 2005], which measures traveltime differences between the envelopes by using cross correlations of the envelope time series for a range of time lags. We relocated the hypocenters using a double-difference method [*Waldhauser and Ellsworth*, 2000] and a velocity model JMA2001. The source locations are shown by red circles in Figure 3 and the sources located at depths of ~30 to ~40 km, which correspond to the regions where the deep low-frequency earthquakes have episodically occurred (yellow circles in Figure 3) above the subducting Philippine Sea plate. The triggered tremor seems to have occurred in five

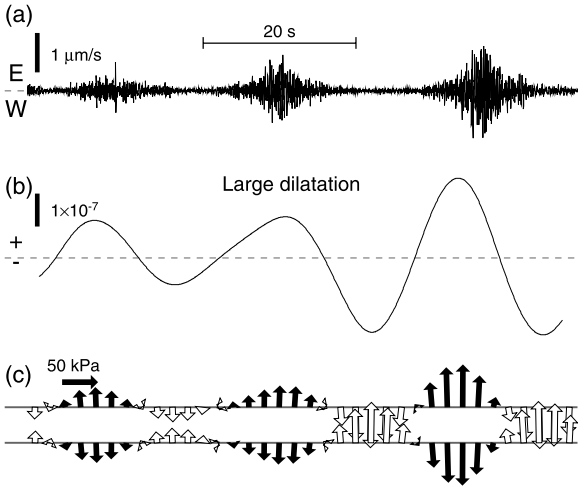

Figure 2. Example of the relationship between triggered deep low-frequency tremor and strain changes in the source region. (a) Time series of vertical seismic activity observed at KWBH (1887–1962 s, in Figure 1). The time is corrected in order to compare to the bottom trace. (b) Dilatation caused by the arriving Rayleigh waves obtained by summing equations (5) and (6). (c) Stress changes on the plate boundary. Black and white arrows indicate expansion and compression, respectively. We assume that the subducting slab has a northwestward dip of 10°. The dip direction is perpendicular to the radial direction from the Sumatra earthquake.

clusters: western and eastern Shikoku, western and central Tokai and the Kii peninsula.

[9] The observations below show that the triggered tremor-like events are deep low-frequency signals that are similar to other reports of slab tremor or low-frequency earthquakes. In order to avoid a premature identification of the physical mechanism of the tremor, we continue to use the term "event" for discrete episodes of tremor with well-defined arrivals. Ultimately, we will identify a continuous episode of tremor with overlapping earthquakes in a model similar to that suggested by *Shelly et al.* [2006].

[10] The spectrum of the triggered events is consistent with other tremor observation and is distinct from any of the features of the seismic waves originating at the main shock. Figure 4 shows an example of the Fourier spectra of vertical and horizontal components from 1400 to 2400 s (see Figure 1) at stations with almost the same epicentral distance from the Sumatra earthquake, KWBH and IKNH, where the tremor has been observed and has not, respectively. The ratios of the same components for two stations are shown in the bottom. The spectra lower than 1 Hz almost correspond to each other, while there are large differences in ranges higher than 1 Hz, which are especially significant in the horizontal component. The isolated tremor spectrum is consistent with other measures of the spectra of episodic deep low-frequency earthquakes showing unusually low frequencies for its amplitude and a roughly $1/f$ frequency decay [*Ide et al.*, 2007b]. (The 20 Hz peak is known contamination due to a borehole resonance).

[11] Like other examples of low-frequency earthquake and tremor, the triggered events generated predominately shear waves as inferred by the apparent velocity and large amplitude in horizontal components (Figures 1 and 5), and had large amplitudes for waves from 1 to 15 Hz (Figure 4). Figure 5 shows the largest tremor observed in western Shikoku as an example. The observed 2–16 Hz waveforms at each epicentral distance are shown for each component. Two dotted curves roughly show P and S wave arrivals, assuming the origin time is 0 on the scale shown. The large wave packets travel at S wave velocity, while we can find arrivals of subtle proceeding signal in vertical components which seem to be on the P wave arrivals. The proceeding signals may be P waves and/or S waves from another

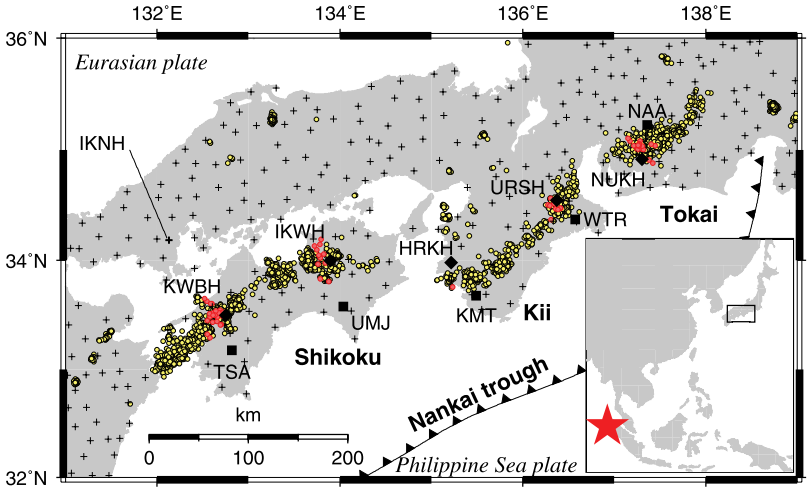

Figure 3. Deep low-frequency (DLF) earthquake distributions in western Japan. The epicenters of the background seismicity from 2000 to 2004 determined by Japan Meteorological Agency (JMA) are indicated by yellow circles. The triggered deep low-frequency tremor is indicated by a red circle. Waveforms observed at Hi-net stations KWBH, IKWH, HRKH, URSH, and NUKH (diamonds) are indicated in Figures 1a and 7. Other Hi-net stations are shown by crosses. TSA, UMJ, KMT, WTR, and NAA (squares) are the broadband seismic (F-net) stations. Inset map shows the geographical relationship between the region (box) and the epicenter of the 2004 Sumatra-Andaman earthquake (star).

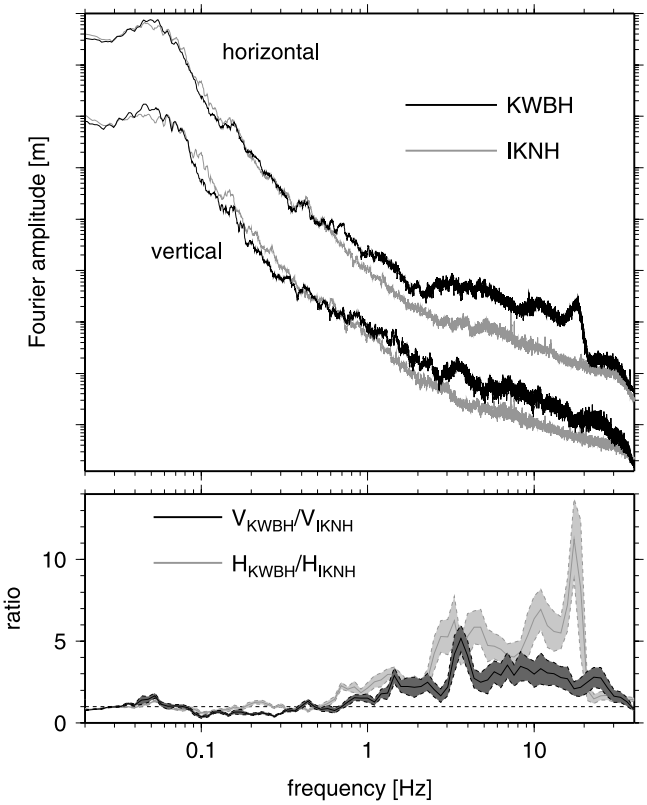

Figure 4. Vertical and horizontal Fourier spectra recorded at KWBH and IKNH. The two stations are indicated in Figure 3. KWBH locates near the epicentral region of the triggered deep low-frequency tremor, while IKNH does not. The time window is from 1400 to 2400 s in Figure 1. A peak around 20 Hz in horizontal component is known noise due to borehole resonance. In the bottom, the ratio of spectrum amplitudes of vertical components, V_{KWBH}/V_{IKNH}, and that of horizontal components, H_{KWBH}/H_{IKNH}, are shown with smoothing and the shading indicator variations of standard deviation. A horizontal dashed line indicates a ratio of 1.

triggered tremor. If the source model of the triggered tremor is equivalent to a double couple model, we can observe *P* waves at the stations located in the compressional/tensional quadrant of the focal mechanism, which are along northwest and southeast directions at some distances at western Shikoku. We do not always observe them for other triggered tremor. As the early phases are still unclear at other stations and are not common to the other smaller triggered tremor, possibly due to poor signal-to-noise ratios, we focus on the later, larger packets by using only horizontal components in waveform analysis.

[12] For some large triggered tremor, the signal-to-noise ratio is high enough to see the horizontal particle motion even in the frequency range around 1 Hz (Figure 6). The vertical amplitudes are as small as $\sim$1 μm/s, which is comparable with the background noise. Their principal axes of the particle motions are NW-SE, WNW-ESE, and N-S, respectively, which are almost perpendicular to the 40 km depth contour line of subducting Philippine Sea plate boundary at each site as estimated from the seismicity, though the event 10 in central Tokai may not be clear. These events may occur on or above the plate boundary. Higher-frequency waves do not show as clear an orientation from the particle motion. The results are consistent with the source mechanism of a deep low-frequency earthquake by *Ide et al.* [2007a].

[13] An interesting feature of the envelope waveform is that the large packets of tremor are almost symmetrical at each station. To see if this is caused by path effects, we looked at large earthquakes (M $\sim$ 4) that occurred in a similar but slightly deeper location (depth $\sim$40 km) near the plate boundary or in the subducting slab. The earthquakes radiated waves with similar frequencies to the tremor, but amplitudes several thousand times larger. For the earthquakes, the onsets of *P* and *S* waves are clear. In contrast, the waveforms of the tremor in Figure 5 show emergent arrivals even at the distant stations and on high-frequency components. This feature distinguishes the tremor from ordinary tectonic earthquake and implies that the triggered tremor likely produces mostly *S* waves in some continuous or repeated process. Since the envelope shape apparently reflects a source process, it suggests that we should analyze the correlation of the tremor amplitude as a continuous function of the incoming seismic wave strains/stresses.

[14] Larger amplitude surface waves generate more abundant and stronger tremor. Figure 7 shows short-period and long-period root-mean-square (RMS) envelope waveforms from representative examples of each of the clusters in Figure 3. The short-period waveforms are constructed from waveforms filtered with a passband of 2–16 Hz and show the activity of triggered events, and the long-period waveforms are the envelope waveforms of Love and Rayleigh waves filtered with a passband of 0.01–1 Hz. In western Shikoku and the central Tokai regions, the tremor is more actively triggered than other three regions. In all areas, the amplitude of Rayleigh waves (gray line) rather than Love waves (dotted line) appears to correlate with the magnitude of large triggered event. In sections 2.2, 2.3, and 2.4, we will attempt to quantify and expand upon this apparent correlation.

[15] An additional source information on triggered tremor comes from the M_w8.1 Tokachi-oki earthquake. Although less spectacular than the larger Sumatra earthquake, it also triggered tremor in the same regions of the subduction zone. Figure 8 shows observed waveforms at western Shikoku from the Tokachi-oki earthquake, where the epicentral distance is about 1400 km. Three peaks of significant tremor indicated by arrows evidently correspond to the peaks of Rayleigh wave envelope (Figure 8). By using the tremor source location [*Miyazawa and Mori*, 2005] we observed the large dilatation at source region for the large signal amplitudes, like shown in Figure 2b.

[16] Clear triggering of tremor by Rayleigh waves occurred in Japan for at least one other distant earthquake, the Solomon Islands earthquake (M_w8.1) of 1 April 2007. The general features are similar to those reported here.

2.2. Strains at Depth

[17] *Miyazawa and Mori* [2006] examined the strains at the triggered tremor source regions estimated by continuing the wave field observed on the surface to depth using a kernel for one cycle of surface waves, and found that triggered tremors were synchronized with large dilatations.

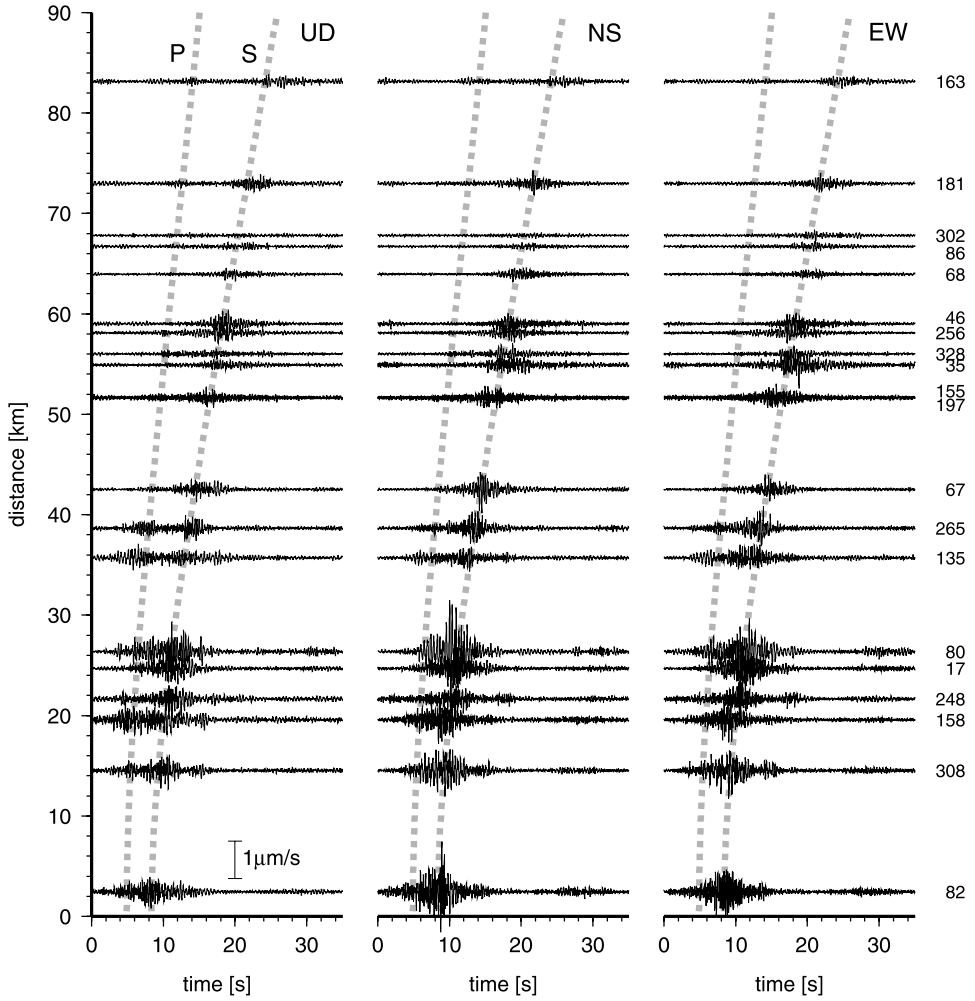

Figure 5. Three-component velocity waveforms (2–16 Hz) of a sample event (western Shikoku event 14 in Figure 7) for epicentral distance. The scale of amplitude is the same for every waveform. Time 0 indicates the origin time of the source that produced the largest peak. Two dotted curves of earlier and later arrivals roughly show *P* and *S* wave traveltime curves, respectively. The station azimuth is indicated in the right margin.

Here we investigate the strains at depth for the full spectrum using appropriate kernels for continuous waveforms.

[18] To extrapolate the observed dilatational strains to depth, we use solutions for Rayleigh wave equation for a simple half-space structure [e.g., *Lay and Wallace*, 1995] and calculate the displacements and then the resulting strains. We only use the fundamental modes as they comprise the components of the strain field that is less

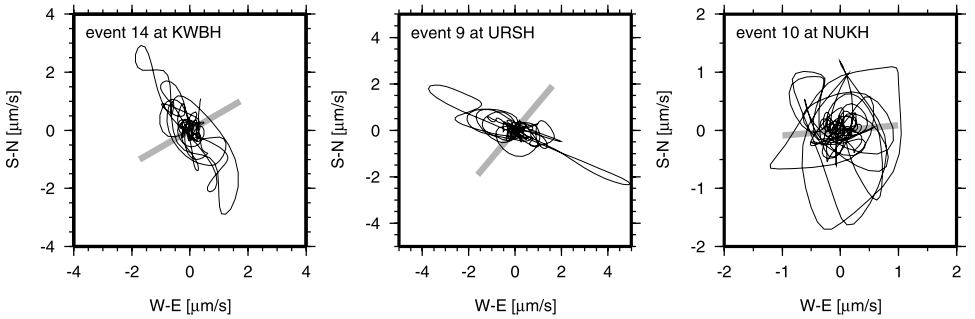

Figure 6. Horizontal particle motions (0.5–2 Hz) of three large triggered events. A gray bold line indicates the direction of the 40 km depth contour of subducting Philippine Sea plate boundary estimated from the seismicity. Events are as numbered in Figure 7: event 14 in western Shikoku, event 9 in western Tokai, and event 10 in central Tokai observed at KWBH, URSH, and NUKH, respectively.

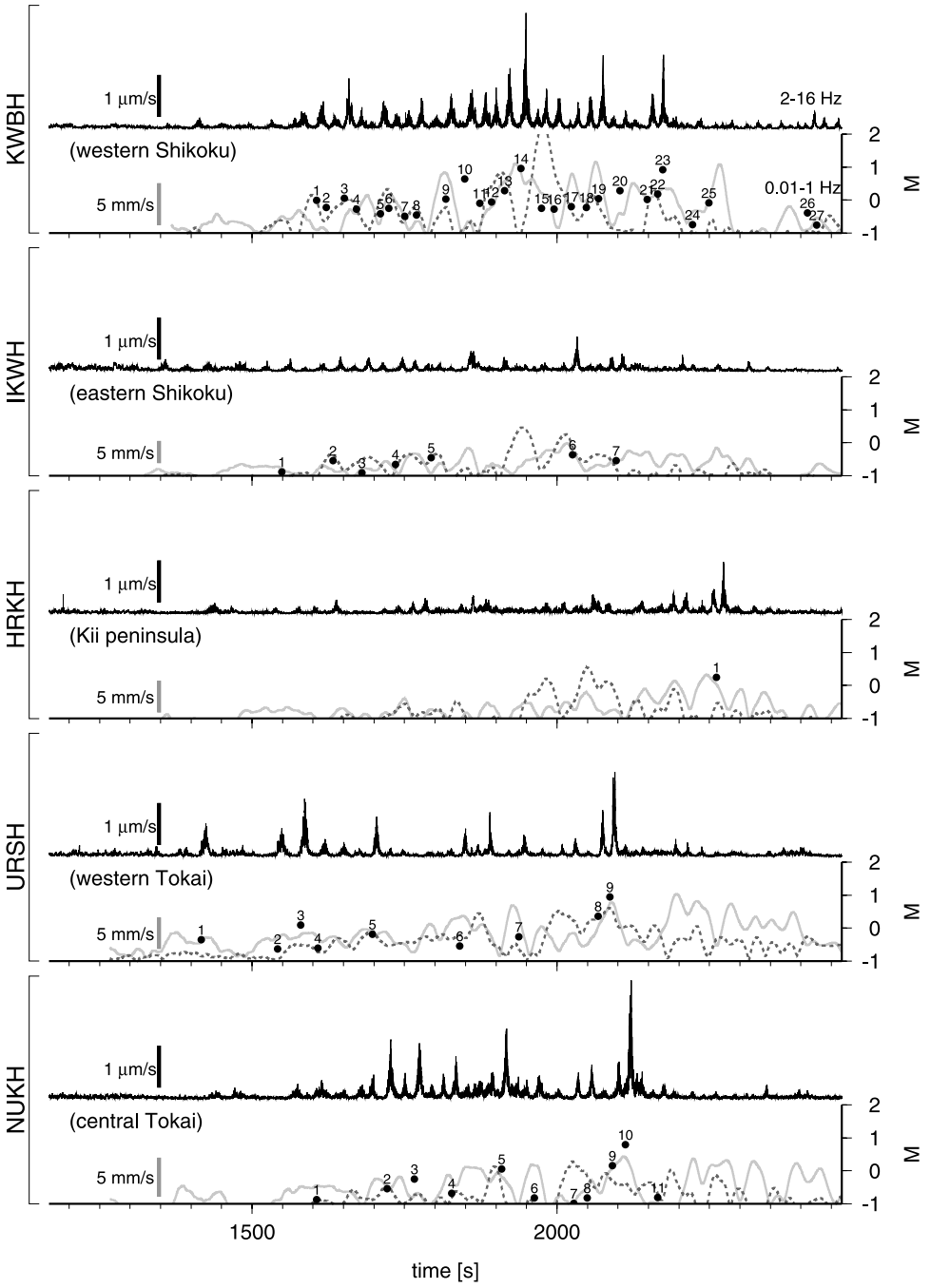

Figure 7. High-frequency (2–16 Hz) root-mean-square (RMS) envelope waveforms (top panels) and magnitude-time graphs with low-frequency (0.01–1 Hz) RMS envelopes of Love and Rayleigh waves observed at the 5 stations KWBH, IKWH, HRKH, URSH, and NUKH (bottom panels). The stations are indicated in Figure 3. The high-frequency envelopes in the solid black lines at the top of each panel are constructed from filtered waveforms from the three components (UD, NS, and EW). The bottom panels show the Love wave envelopes in dashed line from the transverse component and the Rayleigh wave envelopes in gray lines from the vertical and radial components with calibration (see section 2.4). The vertical scale of amplitude is shown at the left portion for each. The bottom panels also include the timing and magnitude of each of the triggered tremor events with magnitudes >-1 in black circles with the origin time based on the largest amplitude signal. The scale of magnitude is labeled in the right vertical axis.

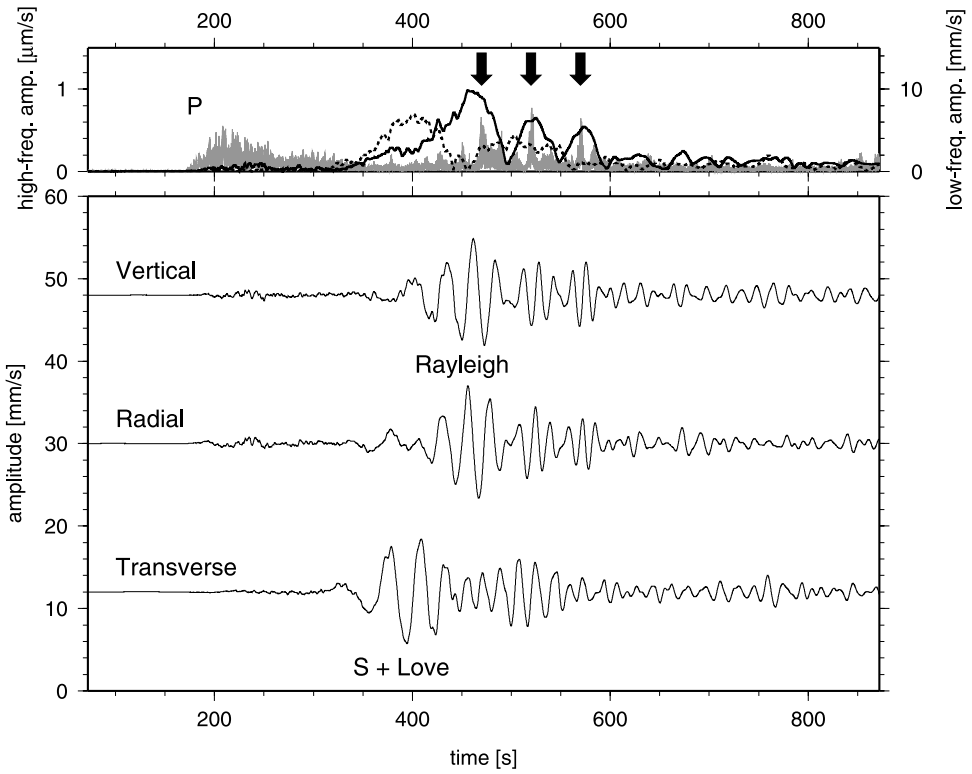

Figure 8. The 2003 Tokachi-oki earthquake (M_w8.1) observed at western Shikoku. The lower three waveforms are observed at TSA and are filtered with a passband of 0.01–1 Hz. (top) Three root-mean-square envelope waveforms. The envelope in gray is constructed by the three-component high-frequency (4–16 Hz) waves observed at KWBH, where the epicentral distance is about 1400 km. The scale of the amplitude is labeled in the left vertical axis. The envelopes in black solid and dashed lines are constructed from the vertical and radial components and transverse component from the Tokachi-oki earthquake, respectively, shown in Figure 8 (bottom). These envelopes in black solid and dashed lines with large amplitudes indicate Rayleigh wave envelope and Love wave envelope, respectively. The scale of amplitude is labeled in the right vertical axis. Zero is the origin time of the Tokachi-oki earthquake (25 September 2003, 1950:08 UT). Three arrows indicate the significant triggering of tremor, which is consistent with the peaks of Rayleigh wave envelope. (bottom) Vertical and radial components and transverse component from the Tokachi-oki earthquake.

sensitive to local structure. We take positive for radial and vertical directions. The normal strain changes across radial and vertical directions are given by

$$e_{rr} = -A_0 k^2 \cos(kr - \omega t) \cdot \left[\exp(-\omega\hat{\eta}_\alpha d) + \frac{1}{2}\left(\frac{c^2}{\beta^2} - 2\right)\exp(-\omega\hat{\eta}_\beta d)\right] \quad (1)$$

$$e_{zz} = A_0 k \cos(kr - \omega t) \cdot \left[c\omega\hat{\eta}_\alpha^2 \exp(-\omega\hat{\eta}_\alpha d) + \frac{\omega}{2c}\left(\frac{c^2}{\beta^2} - 2\right)\exp(-\omega\hat{\eta}_\beta d)\right] \quad (2)$$

respectively, where

$$\hat{\eta}_\alpha = \sqrt{\frac{1}{c^2} - \frac{1}{\alpha^2}}, \quad \hat{\eta}_\beta = \sqrt{\frac{1}{c^2} - \frac{1}{\beta^2}}, \quad (3)$$

A_0 is a constant coefficient, k is the wave number, ω is the angular frequency, r is the radial distance, d is the depth ($z = -d$), α is P wave velocity, β is S wave velocity and c is the phase velocity of the Rayleigh wave. We assume α = 8.7 km/s, β = 5.0 km/s, and c = 3.5 km/s. When we change these velocities within reasonable ranges, the results show little differences. The volumetric strain change $\Delta V/V$ is approximately given by e_{rr} + e_{zz}. Ideally, there is no contribution to e_{rr} and e_{zz}, from Love waves.

[19] To calculate strains beneath a station, we directly estimate the phases and amplitudes from the observed vertical component u_z^{obs} at the surface, while *Miyazawa and Mori* [2006] use only equations (1) and (2) for each cycle of the surface waves. Because the vertical particle motion at the surface is

$$u_z|_{z=0} = A_0 k \cos(kr - \omega t) \cdot \left[c\hat{\eta}_\alpha + \frac{1}{2c\hat{\eta}_\beta}\left(\frac{c^2}{\beta^2} - 2\right)\right], \quad (4)$$

$e_{rr}/(u_z|_{z=0})$ and $e_{zz}/(u_z|_{z=0})$ include neither A_0 nor the sinusoidal function. We obtain the predominant period of the surface wave at arbitrary time to give k and ω, assuming that the period is unique and the surface wave is not dispersed during the cycle. Hence we much more accurately have the computed normal strain changes beneath the station at arbitrary depth as

$$e_{rr} = \frac{e_{rr}^{\mathrm{ref}}}{u_z|_{z=0}} u_z^{\mathrm{obs}} \tag{5}$$

$$e_{zz} = \frac{e_{zz}^{\mathrm{ref}}}{u_z|_{z=0}} u_z^{\mathrm{obs}}, \tag{6}$$

where e_{rr}^{ref} and e_{rr}^{ref} are reference strains e_{rr} and e_{rr} in equations (1) and (2), respectively. Similarly, for the radial particle motion u_r and the vertical particle motion u_z, $\partial u_r/\partial z$ ($=u_{r,z}$) and $\partial u_z/\partial r$ ($=u_{z,r}$) at arbitrary depth are given by $[u_{r,z}/(u_r|_{z=0})]u_r^{\mathrm{obs}}$ and $[u_{z,r}/(u_r|_{z=0})]u_r^{\mathrm{obs}}$, respectively, where

$$\frac{u_{r,z}}{u_r|_{z=0}} = 2\frac{\beta^2}{c^2}\left[\omega\hat{\eta}_\alpha \exp(-\omega\hat{\eta}_\alpha d) + \frac{\omega\hat{\eta}_\beta}{2}\left(\frac{c^2}{\beta^2} - 2\right)\exp\left(-\omega\hat{\eta}_\beta d\right)\right], \tag{7}$$

$$\frac{u_{z,r}}{u_r|_{z=0}} = 2k\frac{\beta^2}{c^2}\left[c\hat{\eta}_\alpha \exp(-\omega\hat{\eta}_\alpha d) + \frac{1}{2c\hat{\eta}_\beta}\left(\frac{c^2}{\beta^2} - 2\right)\exp\left(-\omega\hat{\eta}_\beta d\right)\right], \tag{8}$$

and u_r^{obs} is the observed radial particle motion at the surface. Finally, shear strain change at depth is given by

$$e_{rz} = e_{zr} = \frac{1}{2}\left(\frac{u_{r,z}}{u_r|_{z=0}} + \frac{u_{z,r}}{u_r|_{z=0}}\right)u_r^{\mathrm{obs}}. \tag{9}$$

Examples of the resulting strains and stresses are shown in Figures 2b and 2c for a station KWBH in western Shikoku.

[20] In sections 2.3 and 2.4, we will use these equations to investigate how the event amplitude changes with the amplitude and orientation of strain/stress at the source area. First, we examine the strain changes from the Rayleigh waves in spectra, because many large triggered events seem to be related with the Rayleigh wave amplitude. Then we compare strain amplitudes with triggered event amplitude in five clusters, and compare stress amplitudes with triggered event amplitude with a focus on the best resolved cases in western Shikoku, where the focal mechanism of the tremor source is reasonably well constrained.

2.3. Spectra

[21] After strains are corrected for depth, we can investigate the efficiency of triggering of the wave field as a function of frequency. Since the triggered tremor most clearly occurs during the late Rayleigh waves, we compare the observed triggering during the surface wave train to the Rayleigh waves rather than the Loves waves. In Figures 1 and 2, significant triggering was observed for ~21 s Rayleigh waves around 1900 s, but little triggering occurred at earlier times even though the waves have similar amplitudes in displacement. This may indicate short-period Rayleigh waves are much more capable of exciting deep low-frequency tremor. Both the amplitude and the period of Rayleigh waves may contribute to the volumetric and the normal strain changes at the deep low-frequency source region.

[22] To compute the spectrum of the Rayleigh wave stresses at depth, we start with the Fourier spectra for the ground motion from the Rayleigh waves as recorded at TSA in the broadband seismometer network, F-net (Figures 3 and 9a). The dominant amplitudes are at periods of ~20 s and ~25 s. Clear early arrivals of Rayleigh waves (1400–1500 s in Figure 1) with periods of ~35–50 s also have large amplitudes in displacement. Using equations (1) and (2), we compute the kernels to convert the Rayleigh wave surface motion to strains at the 30 km source depth (Figure 9b). The volumetric strain change $\Delta V/V$ becomes larger for longer period and has a peak value around $T = 50$ s, while e_{rr} and e_{zz} have the large values around $T = 17$–18 s. The sign of e_{rr} changes if the period is longer than 38 s, where the direction of particle motion changes. We then combine the kernel and the observed motion for TSA and each of four other F-net broadband stations representing each of the cluster regions (Figure 9c).

[23] We now want to compare the spectrum of input strains with the spectrum of the strains that effectively trigger tremor. Figure 9d indicates the largest amplitudes of triggered deep low-frequency tremor during the passage of the Rayleigh waves as a function of the corresponding predominant periods. Figure 9d is constructed by taking incoming Rayleigh wave period with the maximum amplitude of the spectra of the time series in a ~100 s moving Gaussian window and plotting it against the amplitude of root-mean-square envelope waveforms of deep low-frequency tremor for the time series in the same window. The indicated period does not necessarily indicate that of the Rayleigh waves which actually triggered the tremor, because secondary peaks may play a role.

[24] In Figures 9c–9d, the peak of surface wave strains at $T \sim 20$ and ~25 s correspond to tremor peaks. For shorter periods, we observed significant deep low-frequency tremor amplitude at $T \sim 17$ s at KWBH, however the corresponding peak in strain is very small. At HRKH, the largest peak appears at shorter period and does not correspond with any peaks of the surface wave spectrum in that region (KMT). For long periods, the maximum volumetric strain change is large for period of $T = 40$ s and greater, but the tremor excited by this period range is small. In the western Tokai region (WTR and URSH), strong triggering has also observed around $T = 34$–38 s where e_{rr} is very small. It seems that, as a function of period, both absolute values of e_{rr} and e_{zz} are more similar to the tremor amplitude than the volumetric strain change. Also, the acceleration (Figure 9a) seems to most closely follow the spectral form of the deep low-frequency signal with strong triggering at short periods and weak triggering at long periods. We conclude that the lack of response at long periods may correspond more closely to

the spectrum of individual components at depth than the dilatation.

2.4. Strain Amplitude and Triggered Amplitude

[25] One way to investigate the quantitative relationship between tremor triggering and surface waves, is to compare the amplitude of the strain components in the Rayleigh waves to the local magnitude. The event magnitude calibration includes attenuation of waves propagating through the structure, and may therefore be an improvement on simply comparing the peak amplitude. Figure 10 shows the relationship between tremor magnitude and the largest volumetric strain change observed during the tremor excitation. The larger amplitude waves seem to be capable of triggering tremor with large magnitude, but small tremor also occurs during the large amplitude surface waves. This is also seen in Figure 7, where some tremor magnitudes are plotted lower than the envelope waveforms. As a result, we could not find a clear relationship with magnitude using this method.

[26] We therefore proceed to investigate the relationship between signals from triggered sources and strain changes. We study the correlation of the tremor with the dilatational strain change ($\Delta V/V$), the shear strain resolved on the fault plane, and the change in the Coulomb failure function change

$$\Delta \mathrm{CFF} = \Delta\tau + \mu(\Delta\sigma_n + \Delta p), \tag{10}$$

where μ is the friction coefficient, $\Delta\tau$ and $\Delta\sigma_n$ are shear stress change resolved in slip direction and normal stress change on the fault plane, respectively, and Δp is pore pressure change. Pore pressure changes are anticorrelated with the normal stress changes with $\Delta p = -B\Delta\sigma_n$ where B is the Skempton coefficient. Therefore the second term of Coulomb failure function change can also be written as $\mu'\Delta\sigma_n$, where $\mu' = (1 - B)\mu$.

[27] We obtain the strain changes ($\Delta V/V$, e_{rr}, and e_{zz}) during the surface waves by using equations (5) and (6) with the appropriate periods and the observed vertical displacement waveforms.

[28] Strain changes at depth from the Love wave are also obtained from *Lay and Wallace* [1995]. We give a slow velocity layer above half-space, where we assume the differences of shear moduli and velocities between the top layer and the lower half-space is small so that the structure is similar to that used for Rayleigh wave. We use the fundamental mode. Then the dispersion equation is approximately given by

$$\frac{\mu_2 \hat{\eta}_{\beta_2}}{\mu_1 \eta_{\beta_1}} = 1, \tag{11}$$

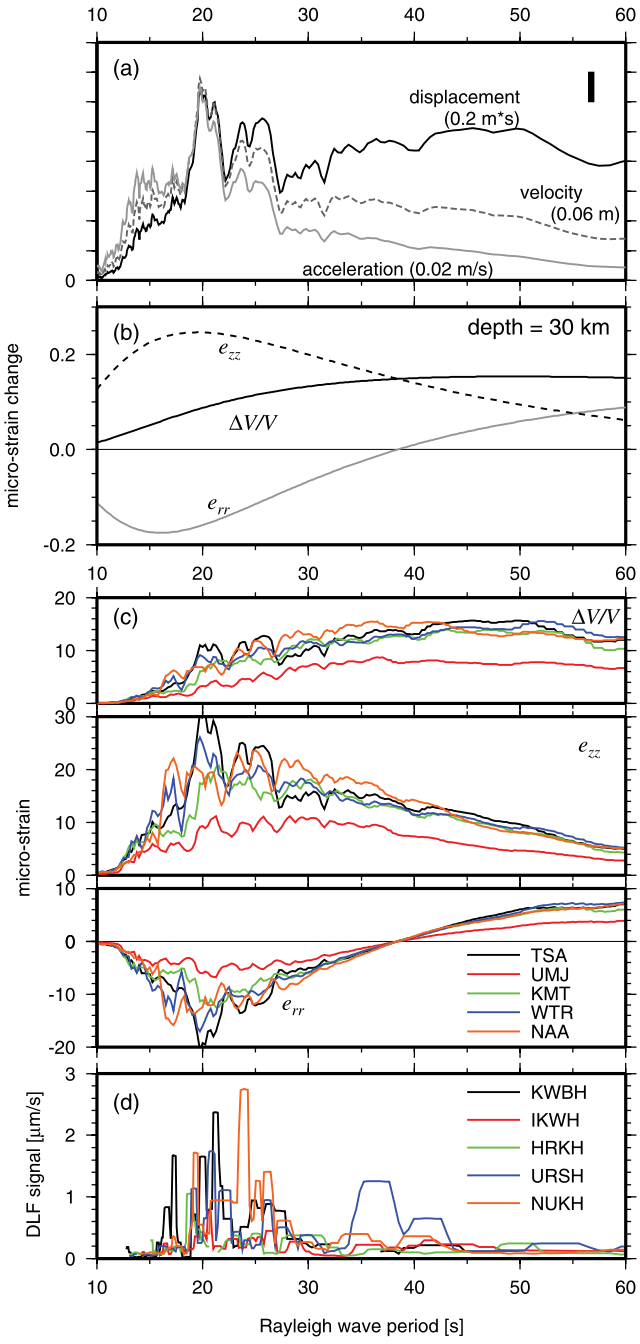

Figure 9. (a) Fourier spectra for the vertical displacement, velocity, and acceleration of Rayleigh waves recorded at TSA. Time window is selected from 1300 to 4000 s. The vertical scale shown at top right portion corresponds to the values indicated in parentheses in each case. The horizontal axis is the period of Rayleigh wave. (b) Largest volumetric strain changes $\Delta V/V$ and corresponding two normal strain changes e_{zz} and e_{rr} (in vertical and radial directions, respectively) at the depth of 30 km, for the function of the period of Rayleigh wave. Amplitudes are normalized by the largest vertical displacement at the surface to demonstrate the depth correction factor (equations (5) and (6)). (c) Relationship between the period of Rayleigh wave and absolute strain changes (top) $\Delta V/V$, (middle) e_{rr}, and (bottom) e_{zz}, from the Rayleigh waves. The curves of TSA are made by combining Figures 9a and 9b. The similar relationships at UMJ, KMT, WTR, and NAA are shown in different colors. Station locations are in Figure 3. (d) Peak amplitudes of triggered deep low-frequency signals at five regions during arrivals of Rayleigh waves, with respect to indicated predominant period. The colors indicate the regions same as shown in Figure 9c (bottom).

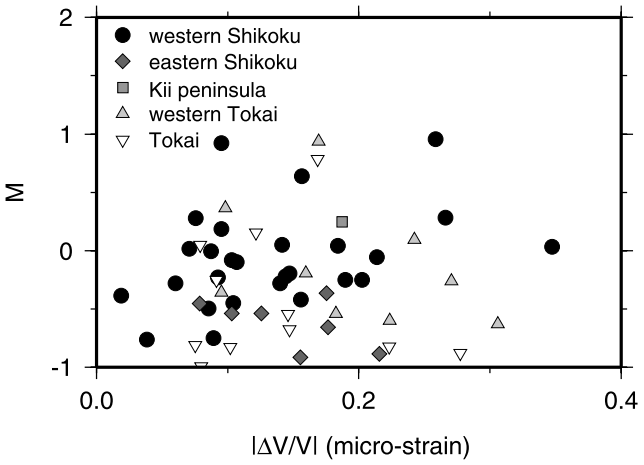

Figure 10. Relationship between local event magnitude and the maximum volumetric strain change.

where μ is shear modulus, $\hat{\eta}$ refers to equation (3), $\eta = i\hat{\eta}$, $\beta_1 < c < \beta_2$ for Love wave velocity c, $\mu_2 = 1.5\ \mu_1$, and suffixes 1 and 2 denote the top layer and the lower half-space, respectively. For the transverse particle motion u_t and the depth $d \geq H$,

$$\frac{u_{t,z}}{u_t|_{z=0}} = \frac{\pi\hat{\eta}_{\beta_2}}{4\sqrt{2}\eta_{\beta_1}H}\exp\left(-\frac{\pi\hat{\eta}_{\beta_2}}{4\eta_{\beta_1}}\frac{d-H}{H}\right) \tag{12}$$

$$\frac{u_{t,r}}{v_t|_{z=0}} = -\frac{k}{\sqrt{2}\omega}\exp\left(-\frac{\pi\hat{\eta}_{\beta_2}}{4\eta_{\beta_1}}\frac{d-H}{H}\right), \tag{13}$$

where H is the thickness of the top layer, $u_t|_{z=0}$ and $v_t|_{z=0}$ are transverse particle motions in displacement and velocity, respectively, at surface. We use $H = 30$ km and calculate the shear strain changes at the same depth. Shear strain changes at depth are given by

$$e_{zt} = e_{tz} = \frac{1}{2}\frac{u_{t,z}}{u_t|_{z=0}}u_t^{\mathrm{obs}} \tag{14}$$

and

$$e_{rt} = e_{tr} = \frac{1}{2}\frac{u_{t,r}}{v_t|_{z=0}}v_t^{\mathrm{obs}}. \tag{15}$$

The normal strain change in transverse direction, e_{tt}, is equal to zero.

[29] We then resolve the stresses on the fault plane and compare the tremor timing with each of the strain components. As shown by *Ide et al.* [2007a], the focal mechanisms of low-frequency earthquakes are consistent with the fault plane being aligned with the subducting slab at western Shikoku. We use the *Ide et al.* [2007a] fault plane solution to resolve the shear stresses and total Coulomb failure stress on the fault plane only in western Shikoku. Seismic waveforms observed at a station above the triggered tremor region would be ideal for this purpose. We use the Hi-net data rather than the F-net data because the denser Hi-net network has more stations very near the triggered deep low-frequency source regions (Figure 3). The Hi-net seismometers have natural periods of 1 s, and they may not be suitable to get the actual particle motions for long-period waves such as from the Sumatra earthquake without additional calibration. By matching the Hi-net records with nearby F-net records, we calculate that the Hi-net amplitudes should be about 4.5 times as large as specified by the standard calibration. We also apply this calibration to make surface wave envelopes in Figure 7 but not in Figure 9 because we cannot calibrate the amplitude for a wide frequency range.

[30] From the determination of the tremor locations shown in Figure 3, the hypocenters appear to locate at almost the same region in each of five clusters. The relocated hypocenters still have significant errors in depth. In sections 2.4.1 and 2.4.2 we consider two possibilities: Either the hypocenters are colocated in each cluster or they are not. We will show that the results are not sensitive to either assumption. As discussed above, we use the horizontal components for the high-frequency observations in order to focus on the clearest, largest packets of triggered tremor for each.

2.4.1. Assuming Tightly Clustered Events

[31] Here we assume that in each cluster of events, individual sources are separated by much less than the wavelength of the incoming surface waves. We use waveforms observed at 5 Hi-net stations shown in Figure 3 (diamonds). The source location is assumed to be the mean location of each cluster.

[32] We then compare the tremor amplitudes with the triggering strain/stress changes by shifting the observed surface waves at the station closest to the epicenter (corrected for depth) to the source location. The time shift is computed by combining the traveltime for the tremor and the phase shift of the surface waves resulting from the propagation from the tremor epicenter to the observation station.

[33] *Miyazawa and Mori* [2006] found that triggering correlated with peak amplitude of volumetric strain changes. When we relocated the hypocenters, the result is almost the same. Figure 11 shows the relationships between the strain changes at the source region and the deep low-frequency signals at the 5 regions. The strain changes span $\pm 3 \times 10^{-7}$. In 4 regions except for the eastern Shikoku region (IKWH), we find a clear relationship that large dilatation excites both large and small tremor signals while the contraction only excites small tremor. At eastern Shikoku, the trends seem to be opposite to the other regions. However, the relocated hypocenters are not robust and include large location errors, because the signal-to-noise ratios are very poor among the 5 regions (Figure 7), and the result may not be resolved. As a result, the mean tremor amplitude generally increases with volumetric strain change (solid line) as does the variance (shaded region).

[34] In Figure 11 (right), the averages of signal amplitudes are fit by two- and three-dimensional polynomials and exponential functions for volumetric strain changes. An n-dimensional polynomial for x is given by $\sum_{i=0}^{n} a_i x^i$, where larger n fits the data better. An exponential function for x is given by $a\ \exp(bx) + c$. The standard deviations of the

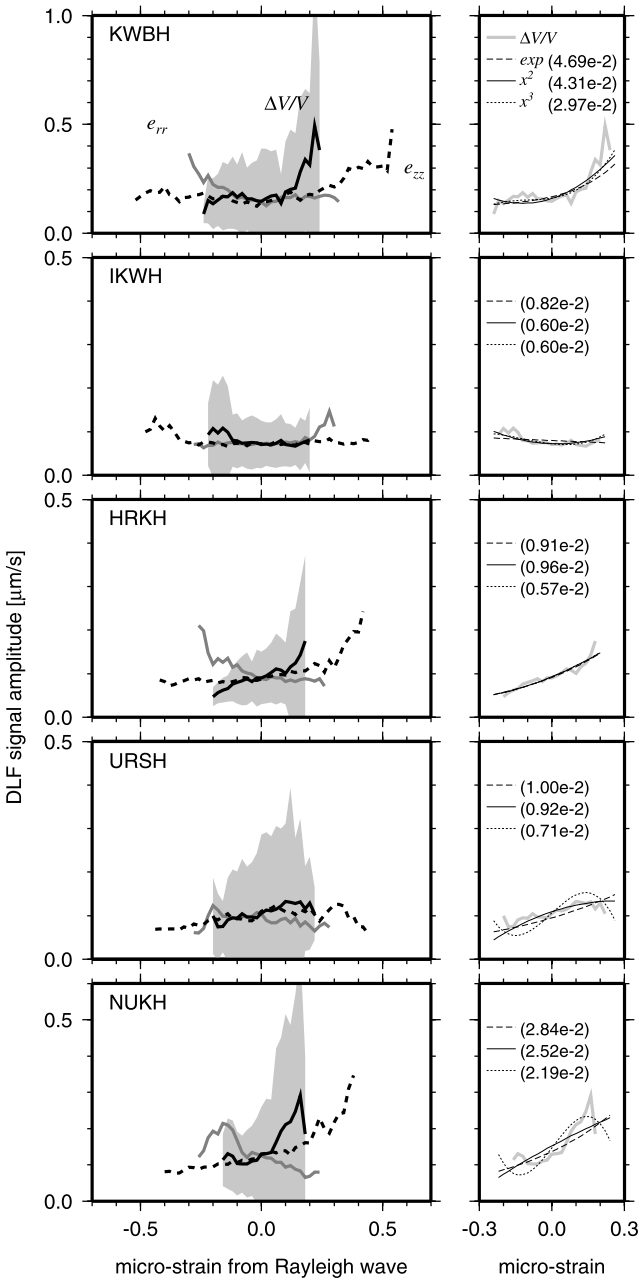

Figure 11. Relationships between the strain changes at the source region and the deep low-frequency signals in horizontal component at five stations distributed over the five event clusters. The time window used for the analysis is from 1300 to 2600 s (see Figures 1 and 7). The vertical axis indicates the signal amplitude of triggered deep low-frequency tremor and the horizontal axis indicates the strain change from Rayleigh wave. The volumetric, vertical normal, and radial normal strain changes are indicated by solid lines with errors, dashed line, and gray line, respectively. The shaded area indicates the standard deviation of residuals of volumetric strain changes. In the right portion the averages of signal amplitudes are fitted by polynomial and exponential functions for volumetric strain changes. The standard deviations (μm/s) of the residuals between the functions and observations are indicated in parentheses.

residuals between the functions and observations are indicated in parentheses. In every region, though the polynomial functions match the observations better, the differences are small. To address the small signal under the compression, the exponential model is also reasonable as the differences between models are small.

[35] Motivated by the correlation between acceleration and tremor spectra in Figure 9, we also obtain the relationship between the vertical acceleration at source regions and the deep low-frequency envelopes at the same 5 stations (Figure 12). We apply the same time shift procedure as above. The acceleration at depth is given by

$$\ddot{u}_z = \frac{\ddot{u}_z^{\mathrm{ref}}}{\ddot{u}_z|_{z=0}} \ddot{u}_z^{\mathrm{obs}}. \tag{16}$$

The values are within ± 1.3 mm/s^2 which is considerably smaller than gravitational acceleration. Because of the phase difference by π from u_z or e_{zz}, the negatively large acceleration corresponds to the large signal amplitude except for IKWH. The standard deviations are large for large mean signal amplitudes and small for small ones. At URSH the peak value does not appear at the negatively largest acceleration as well as in Figure 11. From Figure 9a acceleration and Figure 9d KWBH, the peak values seem to correspond to each other and the acceleration has much better relationship with the event amplitude than dilatation $\Delta V/V$. Nevertheless we find large variances as we did for the dilatation (Figure 11). In Figure 9d we draw the largest amplitude of triggering for period and exclude other small ones, which can cause the amplitude to be variable when we take all the signals into account (Figures 11 and 12). The acceleration may apparently and coincidentally explain the tremor amplitudes well.

[36] We now examine the relationship between the seismic wave stresses and the triggered tremor amplitude (Figures 13 and 14). For this exercise we use examples from western Shikoku where we assume the triggered tremor has the same mechanism as that by *Ide et al.* [2007a]. The Ide et al. mechanism is also consistent with the particle motion of these particular events (Figure 6). We compare the shear stress changes from the Rayleigh and Love waves separately to the triggered signal as well as the composite shear stress, normal stress, and Coulomb failure stress changes. For the purpose of this figure, the Coulomb failure stress change (ΔCFF) is calculated from equation (10) with $\mu' = 0.2$.

[37] There is an obvious and clear correlation between the tremor amplitude and the incoming stresses from the seismic waves. Large, positive stresses that promote shear failure result in large amplitude tremors. This is true for all three of the possible composite stresses (ΔCFF, $\Delta\sigma_n$, and $\Delta\tau$). For the Sumatra earthquake (Figure 13) it is also true for each of the surface waves viewed in isolation. However, for the Tokachi-oki (Figure 14), the Love waves by themselves do not give a strong correlation. This observation motivated some of the earlier work on triggered tremor [*Miyazawa and Mori*, 2006]. The normal stress variations cover a larger range than the shear stresses and thus provide a better resolved function in all cases.

[38] The correlation with all of the components of stress results in an inherent ambiguity in the stress field driving

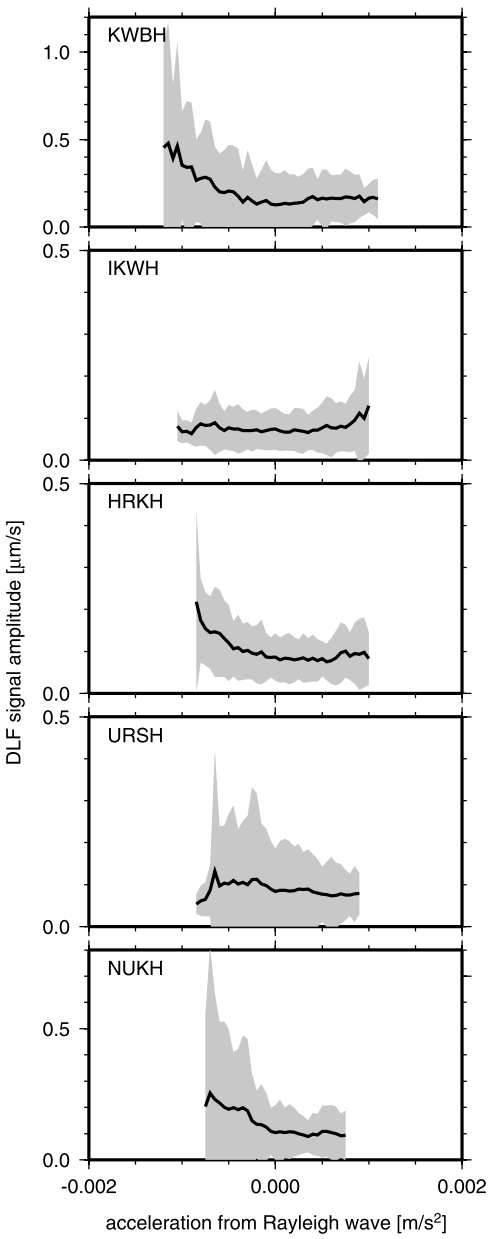

Figure 12. Relationships between the vertical acceleration at the source region and the deep low-frequency signals at five stations. The vertical axis indicates the signal amplitude of triggered deep low-frequency tremor and the horizontal axis indicates the vertical acceleration from Rayleigh wave. The shaded area shows the standard deviation of residuals between the observation and the curve. Time window used for the analysis is from 1300 to 2600 s.

the tremor. To clarify this point, we measure the correlation between the tremor amplitude and the seismic wave stresses as a function of μ' (Figure 15). If the normal stress changes alone are driving the tremor, as originally proposed by *Miyazawa and Mori* [2006], the correlation between the signals should increase with increasing values of μ'. For the Sumatra earthquake, the correlation is high for all physical values of μ' with a slight preference for a very low apparent coefficient of friction (<0.2). Negative values of μ' are also included here to illustrate that the statistical correlation reflects a physical effect that can be only modeled with realistic values of friction.

[39] For the Tokachi-oki earthquake, the total data set shows a relatively weak correlation. However, if the data are limited to the data after the first 450 s of Figure 8, which is after the passage of a long-period Rayleigh wave that did not trigger tremor, the correlation becomes as high as the Sumatra earthquake for any positive value of μ'. In this case, the data weakly prefer the larger values of friction that correspond to a normal stress-controlled triggering. It is worth noting that the Sumatra earthquake also triggered the largest tremor events during the Rayleigh waves late in the wave train rather than during the early Love waves (see Figure 1).

[40] Another complication is that the *S* wave from the Tokachi-oki earthquake also generated large shear stress change along the slip direction with peak amplitudes as much as ~20 kPa. Even though shear stress changes are larger than that from the surface waves, there was no significant triggering at the arrival of *S* waves (Figure 8). Therefore either normal stress control is important or the triggering simply failed to begin into relatively late in the wave train: after both the *S* wave and the long-period Rayleigh waves. For the Sumatra earthquake, there was also no significant triggering by *S* wave (Figure 1) because the generated peak shear stress change along the slip direction is smaller than ~1 kPa because of the fault geometry.

2.4.2. Assuming Multiple Locations

[41] The hypocenters obtained above (Figure 3) still have errors (especially in depth) and it is possible that their separation in each cluster is significant compared with the wavelength of the surface waves. To deal with this possibility, we pursue a different approach to the analysis. Instead of assuming that the pulses colocate, we consider each pulse separately as an individual tremor event that must be shifted in time relative to the others in order to derive the correct phase relationship with the incoming wave. To investigate the relationship as above, we should deterministically give appropriate time shifts for each tremor.

[42] We select well-relocated events with small location errors to minimize the time shift errors. We compare the beginning of the wave packet with a calculated strain change at the source. The symmetric nature of the wave packets and the slowly arising amplitude of the arrivals suggest that the tremor envelopes reflect source time functions (see section 2.1). However, we cannot discount the possibility that the envelope shape after the peak is independent from the effect of the structure during the propagation. Then it is reasonable to correlate the first half packet before the peak with the dilatation in this way. We neglect other factors including path and site effects and radiation patterns, which are unknown. Figure 16 shows the relationships, in which we use the 17 clear deep low-frequency tremor events (9 in western Shikoku, 1 in the Kii peninsula, 2 in western Tokai, and 5 in central Tokai) with large signal-to-noise ratios (for example, see the numbered events in Figure 7).

[43] The tremor amplitudes are large for the positive volumetric dilatation and the vertical expansion, and for the radial compression. The general trend is the same as in

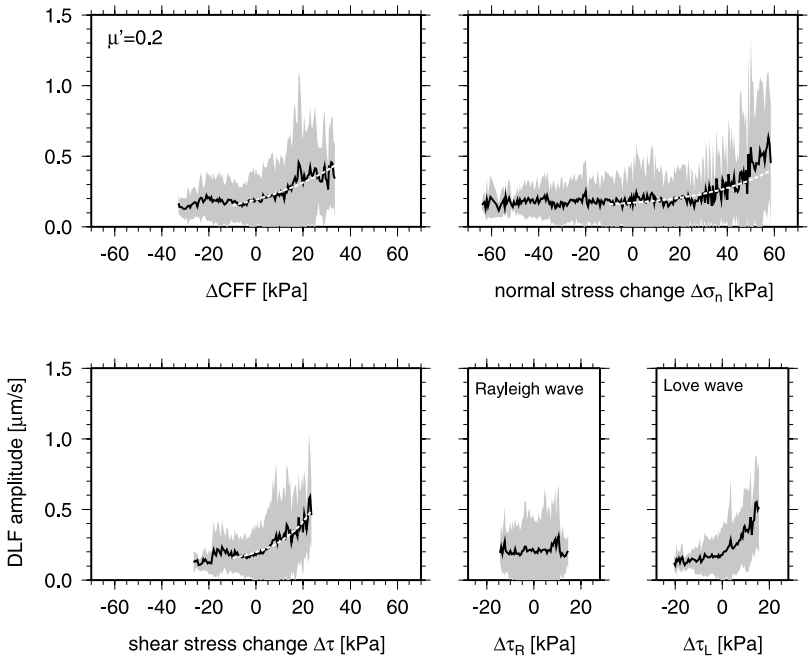

Figure 13. Relationships between triggered signal amplitude and stress changes on the fault plane due to surface waves from the 2004 Sumatra earthquake. ΔCFF is the Coulomb failure stress change, $\Delta\tau$ is shear stress change resolved in the slip direction, and $\Delta\sigma_n$ is normal stress change. $\Delta\tau$ consists of shear stress change from Love wave, $\Delta\tau_L$, and that from Rayleigh wave, $\Delta\tau_R$. The fault mechanism is the same as that of *Ide et al.* [2007a]. The relationships are in black solid lines with errors in shades and some are fit by exponential curves in white dashed lines. Time window is the same as in Figure 11.

Figures 11 and 13. Since the location errors in depth still include about 5 km or more, even though we use the double-difference method for the relocation, the error in the applied time shift may be the cause of the more scattered results. As a result, it is more difficult to discern the exact relationship between triggering strain changes and tremor amplitudes than it was in section 2.4.1. Given the greater error in individual locations, we take the results here to

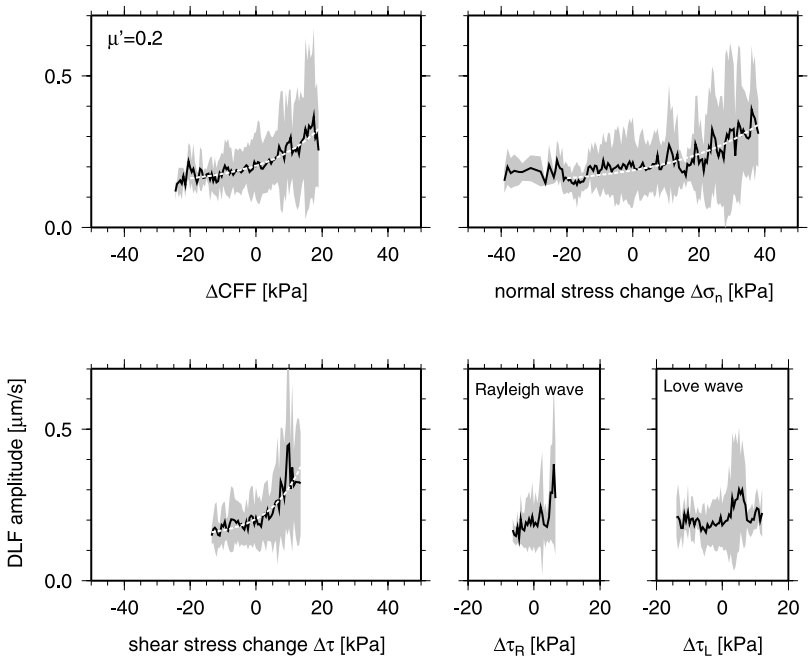

Figure 14. Relationships between triggered signal amplitude and stress changes on the fault plane due to surface waves from the 2003 Tokachi-oki earthquake. Time window used for the analysis is from 350 to 600 s (Figure 8).

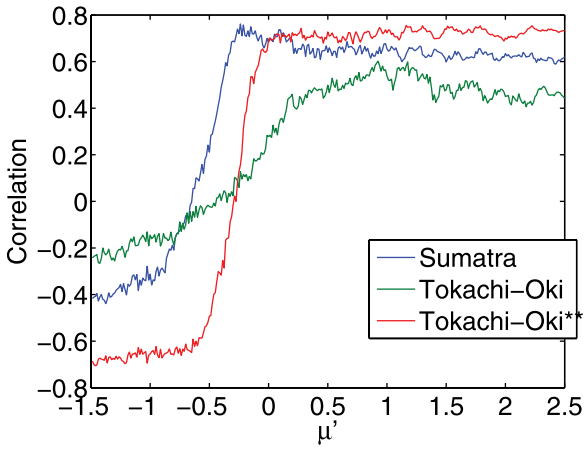

Figure 15. Correlation between the triggered tremor amplitude and the Coulomb failure stress calculated from equation (10) as a function the apparent coefficient of friction μ'. Tokachi-Oki** indicates the correlation with the seismic waves during Tokachi-Oki earthquake beginning at 450 s after the beginning of Figure 8. (See text for rationale.) All correlations are measured with a Spearman rank correlation coefficient which is appropriate for any monotonic function relating the two variables. Negative values of μ' are included to illustrate the poor correlation when a nonphysical model is utilized.

confirm our earlier interpretation with the caveat that the precise relationship between triggering strain changes and tremor amplitude may be much less well constrained if the tremors are not well located.

[44] The stress changes on the fault plane are also calculated as shown in section 2.4.1. We only verify that event 14 at western Shikoku (Figures 2, 5, 6, and 7) has the same source mechanism similar as shown by *Ide et al.* [2007a], although other well-relocated events may also have the similar mechanism. Figure 17 shows the stress changes on the fault plane and the amplitude of the event 14 observed at three stations with the epicentral distances less than 20 km (see Figure 5). (This data set includes KWBH that was featured in Figure 13.) The triggering is correlated with all of the stress changes including ΔCFF. Thus the results of section 2.4.1 are robust to the assumptions about the degree of clustering.

3. Discussion

[45] The key observations of triggered low-frequency tremor are the following:

[46] 1. The low-frequency tremor is triggered by dilatation. This dilatation with the vertical expansion and the radial compression can act directly or via increasing the Coulomb failure stress.

[47] 2. The amplitude of the tremor is an exponential function of the strength of the triggering stresses. Unlike earthquakes, the strength of the tremor appears to be size-predictable. We now pursue the mechanistic implications of these observations.

3.1. Triggering Mechanisms

3.1.1. Coulomb Failure

[48] A simple Coulomb failure model is the most obvious and easiest explanation for the data. The correlation between the tremor amplitude and the resolved Coulomb shear stress change is over 70% for a large range of parameters (Figure 15). Frustratingly, the data are unable to resolve the friction and is highly correlated with the ΔCFF for any positive value of μ'.

[49] The strong correlation with dilatation that was noted in earlier work on the subject is completely consistent with the Coulomb failure model [*Miyazawa and Mori*, 2006]. The dilatation is an important part of the process as it unlocks the fault. The geometry of the fault and the resolved stresses along with the more extreme amplitudes of the Rayleigh waves make them a more direct predictor of failure than the *S* and Love waves in isolation. In particular, the normal stress resolved on the fault plane covers a much larger range of stresses than the shear. The range of normal stresses is about three times larger than that of the shear stresses.

[50] That said, Coulomb failure is not required by the data. A very large coefficient of friction, i.e., normal stress control, is also consistent with the data and even preferred by the Tokachi-oki earthquake (Figure 15). The lack of *S* wave correlation also suggests dilatational control. Given that petrological arguments suggest abundant fluids in the source zone, it is worth investigating whether the normal

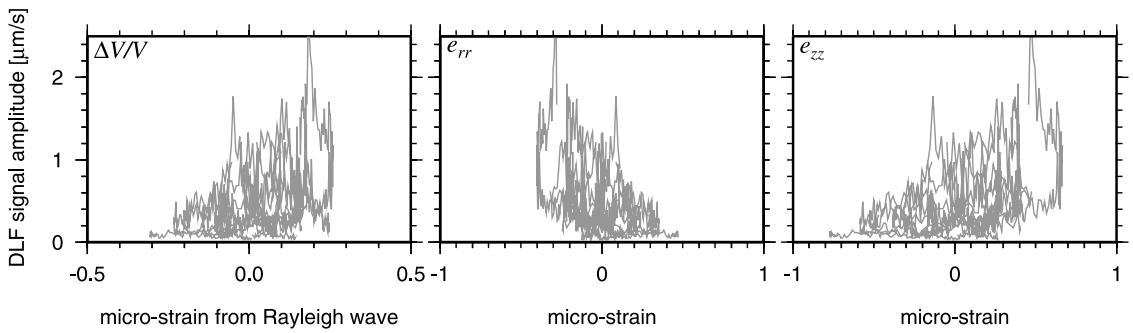

Figure 16. Relationships between 17 signals with small relocation errors and strain changes ($\Delta V/V$, e_{rr}, and e_{zz}). The vertical axis indicates the signal amplitude of triggered deep low-frequency tremor, and the horizontal axis indicates the strain change from Rayleigh wave.

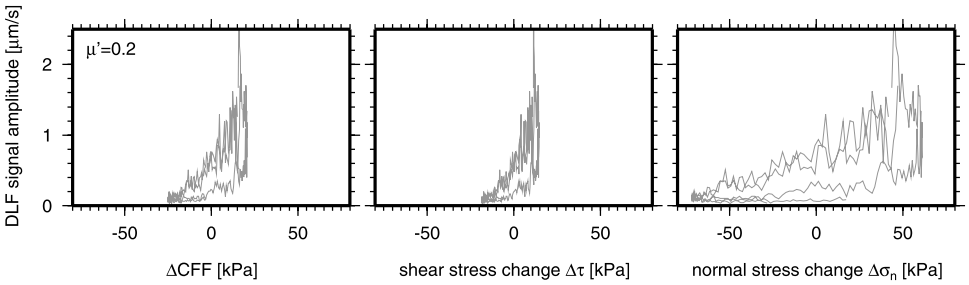

Figure 17. Relationships between amplitudes of event 14 at western Shikoku with stress changes (ΔCFF, $\Delta\tau$, and $\Delta\sigma_n$). Different curves show the relationships observed at the difference stations, where the epicentral distance is smaller than 20 km.

stress might be able to trigger the tremor directly by interacting with the fluid. We pursue this possibility below.

[51] Simple, single process models like Coulomb failure cannot directly address the second major observation of this paper. The models predict failure of an indeterminate size as a result of a strain change, but we observe a correlation between amplitude of the triggered large event and the amplitude of dilatational strain and normal stress changes is demonstrated in Figures 11, 13, 14, and 15. As discussed below, this problem can be solved by introducing a distribution of triggered events.

3.1.2. Tensile Failure

[52] Dilatation exciting tremor might be explained if the source model of the deep low-frequency tremor is a tensile (mode I) crack. However the deep low-frequency tremor mainly produces shear waves. The opening crack is capable of producing shear waves but the amplitude is smaller than or comparable to *P* waves. We could not find strong evidence that the observed waves included dominant *P* waves. Therefore a shear stress in the source seems to be required.

3.1.3. Permeability Pumping

[53] *Miyazawa and Mori* [2006] suggest that the correlation of extensional stresses to the triggered tremor is a fingerprint of fluid flow, which weakens the friction of fractures, where the fluid is dehydrated from subducting slab. Our more thorough statistical analysis does not require such a model anymore, nor does it rule it out (see Figure 15). The normal stresses or dilatations still provide an adequate prediction of the occurrence of tremor. Therefore we flesh out the potential physics of such a mechanism below to provide a basis for testing the scenario that the geometry of future earthquakes allow us to resolve the distinction in stresses.

[54] Compressional normal strain change tends to close cracks and prevents fluid flow; expansion tends to open cracks and increases flow. In fracture-dominated systems, fluid flow rates are very sensitive to crack aperture. For instance, for infinite planar cracks in an otherwise impermeable medium, the permeability is proportional to b^3, where b is the aperture [*Snow*, 1969]. Therefore the dilatation of the seismic waves can generate an oscillation of permeability and thus pump an oscillatory flow. The flow of fluid into a dry fault zone can then weaken the surface by increasing the pore pressure (equation (10)) and/or by suddenly reducing the friction coefficient on the fault, and promote shear failure (Figure 18). Also the increasing normal stress on the fault plays an important role. The dilatation determines the volume of the fluid injected into the fault region. Thus the dilatation as well as increasing normal stress may control the area of failure and hence the magnitude of the resulting slip event.

[55] This fluid-related process can explain why large shear stress change from *S* wave cannot independently trigger the tremor even though this can also enlarge ΔCFF for the Tokachi-oki earthquake. During the arrival of the *S* wave, the amplitudes of the normal strain changes are very small.

[56] This model is similar some ways to that proposed for long-range earthquake triggering by *Brodsky and Prejean* [2005]. Interestingly, the stresses inferred in Figures 13 and 14 are similar to the stresses necessary to trigger crustal earthquakes in Long Valley.

3.2. Distribution of Sources

[57] The problem of increasing stress increasing the amplitude of the tremor can also be addressed by considering a distribution of faults. Some faults might be closer to failure than others. Small strain changes will only affect the faults near failure while larger strain changes will affect both the ones far and near failure. Here we consider the failure as a function of the normal stress changes as they are the largest perturbing stresses in Figures 13 and 14. An analogous calculation can be done for the shear stresses.

[58] The nearly exponential dependence of signal amplitude on the input stresses implies an exponential distribution of failure stress, i.e., if the shear stresses on faults are distributed such that for stresses σ less than the critical stress σ_c

$$n(\sigma) = C_1 \exp\left(C_2 \frac{\sigma_c - \sigma}{\sigma_c}\right), \tag{17}$$

where $n(\sigma)$ is the number of faults with stress σ and C_1 and C_2 are constants, then the number of faults triggered by a change in effective stress $\Delta\sigma$ is found by integrating equation (17) from $\sigma_c - \Delta\sigma$ to σ_c. The result is

$$N(\Delta\sigma) = C_1 \frac{\sigma_c}{C_2}\left[\exp\left(C_2 \frac{\Delta\sigma}{\sigma_c}\right) - 1\right], \tag{18}$$

where $N(\Delta\sigma)$ represents the relative fault area in a particular stress state. The observed tremor is the constructive sum of all the failure signals, so the more area that fails, the higher

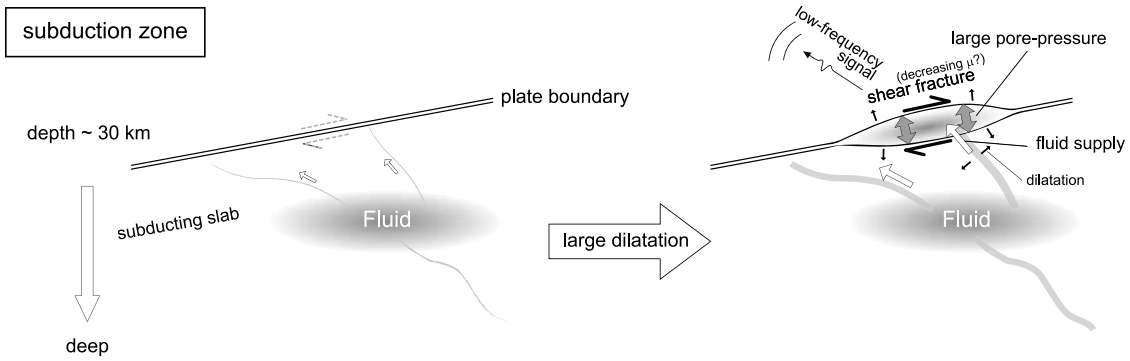

Figure 18. Schematic of permeability pumping mechanism in vertical cross section. On the left, the background at the depth of about 30 km in subduction zone is indicated. Fluid dehydrated from subducting slab is sometimes supplied to plate boundary, which causes low-frequency events. Because of the large dilatation, the aperture of the fluid path opens, and much fluid is supplied into the plate boundary, where the large pore pressure and normal stress change promotes the shear fracture. The low-frequency signal is radiated from the slip.

the amplitude of the resulting tremor. The parameters $C_2/\sigma_c = 3.40 \times 10^{-5}$ and 3.61×10^{-5} Pa^{-1} for normal stress changes at KWBH in Figures 13 and 14, respectively. At other three stations (HRKH, URSH, and NUKH), we also have the same ordered value inferred from the exponential curves in Figure 11, while at IKWH the average of triggering amplitudes against background noise is too poor to obtain some relationships. This distribution approach is similar to that taken by *Dieterich* [1994] and results in a similar distribution of failure strengths.

[59] To relate equation (18) to the rate state model, we can identify σ_c/C_2 with $A\sigma$, where A is an empirically derived constant and σ is the background stress. *Dieterich* [1994] derives seismicity rate change as a function of shear stress change divided by $A\sigma$ and the effective stress changes described here produce the similar effect. The combined value of $A\sigma$ of about 10^4 Pa is similar to that inferred from crustal triggering studies [e.g., *Toda and Stein*, 2003], but the much greater depth of the triggering poses a problem. If A is a nearly constant material property of order 10^{-3}, then the background effective stress must be nearly 2 orders of magnitude below the lithostatic pressure at 30 km. Such a scenario would require extraordinarily high fluid pressures, so fluids would still be a key to the triggering process.

[60] Once the strain energy has been released, the triggering sequence is not expected at the same region unless some strain energies remain. The variable strength of the tremor as a result of identical strains/stresses in Figures 10, 11, 13, and 14 may indicate the possibility that each deep low-frequency tremor has slightly different hypocenter. There may be many strong and weak (or large and small) asperity regions, where the large and small strain energies, respectively, are to be released relatively slowly. The smaller dilatation is capable of moving smaller amount of fluid and triggering tremor, while the larger dilatation is capable of moving larger amount of fluid, providing high and various opportunities for the fluid to contact with both high- and low-strain preexisting regions to cause much larger tremor. This possibly is one of the reasons to explain large variance for large dilatations in Figure 11.

3.3. Nature of Slip

[61] In all of the proposed mechanisms, the low-frequency nature of the seismic signals is controlled by the slip process rather than the fluid flow. The frequency of shear failure events with a given seismic moment is determined by the stress drop and rupture velocity. If either quantity is unusually low, the seismograms will appear low-frequency for their amplitude. From spectra in Figure 4, it is difficult to estimate the corner frequency, but original waveforms show the tremor of ~1 Hz on which high frequency (<15 Hz) waves are superimposed. Using these observations, we could not conclude which factor contributes to the generation of low-frequency waves.

[62] Another clue to the origin of the low-frequency signals is that deep low-frequency events in western Japan and the similar episodic tremor-and-slip (ETS) event found in Cascadia subduction, where the feature of tremor is similar to the deep low-frequency event, have been observed accompanied with the slow slip events in each region [*Obara et al.*, 2004; *Rogers and Dragert*, 2003], suggesting that the phenomenon occurs at the aseismic-seismic transition. In the rate state framework, the transition is where the slip is stable, $A \approx B$. If rupture velocities or stress drops are low in this transitional region, the slip events would radiate unusually long-period waves for their magnitudes.

[63] There are observations of deep low-frequency earthquakes related to slower strain changes [e.g., *Obara et al.*, 2004; *Miyazawa and Mori*, 2005; *Obara and Hirose*, 2006]. *Kao et al.* [2006] propose that episodic tremor-and-slip events are excited by the procedure that dilatational strain field changes due to slow slip on the plate boundary cause fluid migration and excite the events. This observation relating quasi-static deformation to low-frequency tremor reinforces our connection of the triggered tremor to strain, rather than acceleration. We observed clear triggering when the normal strain changes are at least on the order of 10^{-8}.

4. Conclusions

[64] Pulsating triggering of deep low-frequency tremor was observed in western Japan during arrivals of the

Rayleigh waves from the 2004 Sumatra-Andaman earthquake. The significant triggering is coincident with the large dilatation and thus large Coulomb failure stresses at the source region ~30 km deep. Short-period (15–30 s) Rayleigh waves triggered the events much more strongly than the first arrival long-period (>40 s) ones. Larger input stresses result in larger amplitude tremor. The shape of the tremor packets alone indicates that the tremor amplitude is predictable based on the strength of the incoming waves. More detailed analysis suggests that the mean amplitudes of triggered events increase exponentially with the strain change.

[65] Mechanistically, the data are entirely consistent with tremor being generated by a series shear failures triggered by Coulomb failure. However, nothing in this particular data set lets us rule out more direct dilatation control of shear slip via permeability pumping where the expansion increases permeability and thus fluid flow to the fault resulting in slip. In either case, a distribution of sources can reproduce the correlation between the input stresses and the resulting amplitudes of the waves. In the case of a permeability pumping, the amplitude correlation may also happen directly for a single fracture due to the strong dependence of permeability on the dilatation. We are left with an array of possibilities and several useful tests for future triggering episodes to ultimately determine the source of the deep low-frequency tremor.

[66] **Acknowledgments.** Discussion with N. Beeler, H. Kanamori, J. Mori, J. Rubinstein, and J. Vidale helped develop this study. We thank National Research Institute for Earth Science and Disaster Prevention (NIED) for Hi-net and F-net data and Japan Meteorological Agency (JMA) for the earthquake catalog. We use hypoDD [*Waldhauser*, 2001] for the event relocation. The comments from reviewers David Hill and Heather Savage, and Associate Editor Steve Cohen improved the document. This study was supported by Grant-in-Aid for Young Scientists (B) 19740275, MEXT, Japan.

References

Brodsky, E. E., and S. G. Prejean (2005), New constraints on mechanisms of remotely triggered seismicity at Long Valley Caldera, *J. Geophys. Res.*, *110*, B04302, doi:10.1029/2004JB003211.

Dieterich, J. (1994), A constitutive law for rate of earthquake production and its application to earthquake clustering, *J. Geophys. Res.*, *99*, 2601–2618.

Harrington, R. M., and E. E. Brodsky (2007), Volcanic hybrid earthquakes that are brittle-failure events, *Geophys. Res. Lett.*, *34*, L06308, doi:10.1029/2006GL028714.

Ide, S., D. R. Shelly, and G. C. Beroza (2007a), Mechanism of deep low frequency earthquakes: Further evidence that deep non-volcanic tremor is generated by shear slip on the plate interface, *Geophys. Res. Lett.*, *34*, L03308, doi:10.1029/2006GL028890.

Ide, S., G. C. Beroza, D. R. Shelly, and T. Uchide (2007b), A scaling law for slow earthquakes, *Nature*, *447*, 76–79, doi:10.1038/nature05780.

Kao, H., S.-J. Shan, H. Dragert, G. Rogers, J. F. Cassidy, K. Wang, T. S. James, and K. Ramachandran (2006), Spatial-temporal patterns of seismic tremors in northern Cascadia, *J. Geophys. Res.*, *111*, B03309, doi:10.1029/2005JB003727.

Lay, T., and T. C. Wallace (1995), *Modern Global Seismology*, 521 pp., Academic, San Diego, Calif.

Miyazawa, M., and J. Mori (2005), Detection of triggered deep low-frequency events from the 2003 Tokachi-oki earthquake, *Geophys. Res. Lett.*, *32*, L10307, doi:10.1029/2005GL022539.

Miyazawa, M., and J. Mori (2006), Evidence suggesting fluid flow beneath Japan due to periodic seismic triggering from the 2004 Sumatra-Andaman earthquake, *Geophys. Res. Lett.*, *33*, L05303, doi:10.1029/2005GL025087.

Obara, K. (2002), Nonvolcanic deep tremor associated with subduction in southwest Japan, *Science*, *296*, 1679–1681, doi:10.1126/science.1070378.

Obara, K. (2003), Time sequence of deep low-frequency tremors in the southwest Japan subduction zone: Triggering phenomena and periodic activity (in Japanese with English abstract), *J. Geogr.*, *112*, 837–849.

Obara, K., and H. Hirose (2006), Non-volcanic deep low-frequency tremors accompanying slow slips in the southwest Japan subduction zone, *Tectonophysics*, *417*, 33–51, doi:10.1016/j.tecto.2005.04.013.

Obara, K., H. Hirose, F. Yamamizu, and K. Kasahara (2004), Episodic slow slip events accompanied by non-volcanic tremors in southwest Japan subduction zone, *Geophys. Res. Lett.*, *31*, L23602, doi:10.1029/2004GL020848.

Omori, S., K. Komabayashi, and S. Maruyama (2004), Dehydration and earthquakes in the subducting slab: Empirical link in intermediate and deep seismic zones, *Phys. Earth Planet. Inter.*, *146*, 297–311, doi:10.1016/j.pepi.2003.08.014.

Prejean, S. G., D. P. Hill, E. E. Brodsky, S. E. Hough, M. J. S. Johnston, S. D. Malone, D. H. Oppenheimer, A. M. Pitt, and K. B. Richards-Dinger (2004), Remotely triggered seismicity on the United States West Coast following the Mw 7.9 Denali fault earthquake, *Bull. Seismol. Soc. Am.*, *94*, S348–S359, doi:10.1785/0120040610.

Rogers, G., and H. Dragert (2003), Episodic tremor and slip on Cascadia subduction zone: The chatter of silent slip, *Science*, *300*, 1942–1943.

Rubinstein, J. L., J. E. Vidale, J. Gomberg, P. Bodin, K. C. Creager, and S. D. Malone (2007), Non-volcanic tremor driven by large transient shear stresses, *Nature*, *448*, 579–582, doi:10.1038/nature06017.

Shelly, D. R., G. C. Beroza, S. Ide, and S. Nakamula (2006), Low-frequency earthquakes in Shikoku, Japan, and their relationship to episodic tremor and slip, *Nature*, *442*, 188–191, doi:10.1038/nature04931.

Snow, D. (1969), Anisotropic permeability of fractured media, *Water Resour. Res.*, *5*, 1273–1289.

Toda, S., and R. Stein (2003), Toggling of seismicity by the 1997 Kagoshima earthquake couplet: A demonstration of time-dependent stress transfer, *J. Geophys. Res.*, *108*(B12), 2567, doi:10.1029/2003JB002527.

Toriumi, M., and M. Inui (2001), Pressure-temperature-water production rate paths in the subduction metamorphism, *Bull. Earthquake Res. Inst. Univ. Tokyo*, *76*, 367–376.

Waldhauser, F. (2001), hypoDD—A program to compute double-difference hypocenter locations, *U.S. Geol. Surv. Open File Rep., 01-113*.

Waldhauser, F., and W. L. Ellsworth (2000), A double-difference earthquake location algorithm: Method and application to the northern Hayward fault, California, *Bull. Seismol. Soc. Am.*, *90*, 1353–1368, doi:10.1785/0120000006.

West, M., J. J. Sanchez, and S. R. McNutt (2005), Periodically triggered seismicity at Mount Wrangell, Alaska, after the Sumatra earthquake, *Science*, *308*, 1144–1146, doi:10.1126/science.1112462.

E. E. Brodsky, Department of Earth Sciences, University of California, Santa Cruz, CA 95060, USA. (brodsky@pmc.ucsc.edu)

M. Miyazawa, Disaster Prevention Research Institute, Kyoto University, Uji, Kyoto 611-0011, Japan. (linen@eqh.dpri.kyoto-u.ac.jp)